# Coupling of Fe and uncompensated Mn moments in exchange-biased Fe/MnPd

Sebastian Brück*
*Physikalisches Institut, Universität Würzburg, D-97074 Würzburg, Germany*
*and Max-Planck-Institut für Metallforschung, D-70569 Stuttgart, Germany*

Sebastian Macke and Eberhard Goering
*Max-Planck-Institut für Metallforschung, D-70569 Stuttgart, Germany*

Xiaosong Ji, Qingfeng Zhan, and Kannan M. Krishnan†
*Department of Materials Science and Engineering, University of Washington, Seattle, Washington 98195, USA*
(Received 4 January 2010; published 9 April 2010)

A bilayer exchange-bias system composed of Fe/MnPd is investigated using x-ray magnetic circular dichroism (XMCD) and soft x-ray resonant magnetic reflectometry (XRMR). The absorption and XMCD data at the Fe *L* and Mn *L* edges are used to derive the optical and magneto-optical properties of the individual layers. Then the structural and magnetic depth profiles of the sample are obtained from XRMR. From reflectivity measurements at the Fe *L* and Mn *L* edges, a precise magnetic depth profiling of the interface region between the ferromagnet (F) and antiferromagnet (AF) was carried out. It reveals rotatable and pinned uncompensated Mn moments in the AF. By comparing the signs and magnitudes of the absorption, the relative coupling directions in the system are determined. It is found that rotatable Mn and the ferromagnetic Fe couple antiparallel. The pinned Mn moments are oriented antiferromagnetic to the neighboring rotatable Mn and ferromagnetic with respect to the Fe during the field cooling process.

DOI: 10.1103/PhysRevB.81.134414 PACS number(s): 75.30.Et, 75.70.−i, 78.20.Ls, 61.05.cm

## I. INTRODUCTION

Exchange bias is a unidirectional anisotropy observed in ferromagnet (F)/antiferromagnet (AF) systems (for recent reviews see, e.g., Refs. 1–3). The term exchange bias usually refers to the loop shift observed for the hysteresis of the F when it is in direct contact to an AF after the whole system has been field cooled through the ordering temperature of the AF. During the field cooling procedure, the F imprints a preferred direction into the AF (Refs. 4 and 5) and thereby causes the unidirectional anisotropy. Besides the loop shift, an increase in the coercive field of the F is also observed in such systems. While the former is attributed to pinned uncompensated moments in the AF (see, e.g., Refs. 1–3), it is assumed that the coercive field increase is related to rotatable moments in the AF.[3] The existence of rotatable uncompensated moments directly at the F/AF interface has been proven for a broad variety of exchange-bias systems.[6–12] A direct detection of pinned uncompensated moments is however more demanding (see, e.g., Refs. 13 and 14) and their exact location in the AF was just recently derived for a nonmetallic[15] and a metallic[11] AF. In both latter cases, x-ray resonant magnetic reflectometry (XRMR) was used to determine the position of pinned and rotatable moments in the system. XRMR is a combination of conventional chemical depth profiling x-ray reflectometry and x-ray magnetic circular dichroism (XMCD) which introduces an additional magnetic contrast. This technique provides structural and magnetic depth profiles at a very high spatial resolution of ~1 Å (Ref. 16) in an element selective way making it the perfect tool for the investigation of exchange-bias systems. Here we present a detailed study which resolves the relative coupling directions of all three kinds of magnetic moments in an epitaxially grown, metallic, exchange-biased thin-film sample: the F, the rotatable moments in the AF, and the pinned moments in the AF.

## II. EXPERIMENTAL

A bilayer sample with nominal thickness of $Mn_{52}Pd_{48}$(750 Å)/Fe(85 Å)/Pt(15 Å) was grown epitaxially on a MgO(001) substrate in an ultrahigh vacuum ion-beam sputter deposition system with a base pressure of $10^{-9}$ mbar. The substrate was cleaned by acetone and ethanol before mounting it in the preparation chamber. Prior to film deposition the substrate was degassed at 500 °C for 1 h to remove any adsorbent from the surface. During the film growth, the substrate temperature was kept at 85 °C which results in a chemically disordered MnPd layer. To chemically order the system and establish a well-defined crystallography with the *a*-axis pointing normal to the surface, the sample was annealed at 250 °C for 1 h in vacuum.[17] During this procedure, a magnetic field was applied to establish a well-defined exchange-bias direction in the film. After preparation, the crystallographic *a*-axis orientation of the MnPd film was checked by x-ray diffraction and led to results similar to the one shown in Ref. 18. Room-temperature vibrating sample magnetometry (VSM) was used to characterize the magnetic properties of the sample, i.e., the exchange bias, coercive field, and necessary saturation fields. The resulting VSM hysteresis of the sample is shown in Fig. 1. A shifted loop with an exchange bias, $H_{eb}=-4.8$ mT and a coercive field, $H_C=13$ mT is found from the measurement. The VSM hysteresis also shows that a field of 60 mT is sufficient to fully saturate the sample at room temperature. The sample was investigated by XMCD and XRMR at the APPLE II type undulator beamline UE56/2-PGM1 at BESSY II in Ber-

 

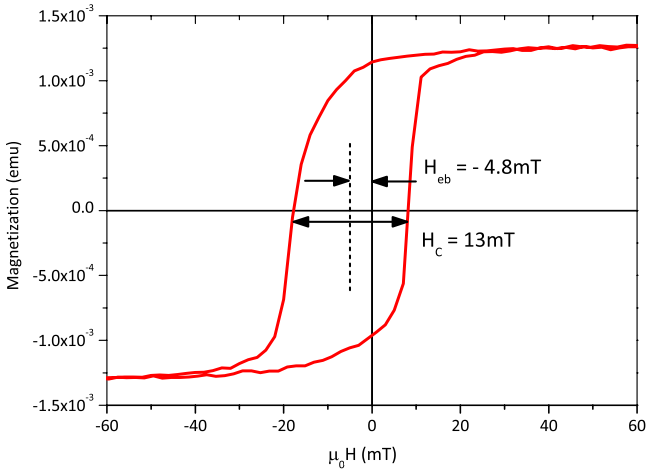


FIG. 1. (Color online) $M(H)$ hysteresis measured at room temperature using a vibrating sample magnetometer and with the external field aligned along the exchange-bias direction.

lin, Germany. For both, XMCD and XRMR measurements, a new dedicated experimental setup was used.[19] This instrument consists of a two-circle goniometer with a 360° rotatable sample stage and a detector stage to measure the specular reflection. An independently rotatable magnetic yoke provides a fast switchable magnetic field of up to 200 mT at the sample position in the scattering plane. Besides reflectivity, x-ray absorption spectra can also be measured by both total electron yield (TEY) and total fluorescence yield (TFY). More details on the experiment are described elsewhere.[19] The analysis of the measured reflectivity curves, nonmagnetic or with magnetic contrast, is complicated by the fact that such spectra cannot be back transformed analytically to obtain the underlying optical or magneto-optical profile. Instead, an iterative simulation approach is used: the expected reflectance is calculated using a magneto-optical approach and the obtained reflectivity curve is compared to the measured one. The parameters are then refined until a good convergence between the measurement and simulation is reached. During the last years we have developed a software tool called REMAGX which is especially dedicated to fitting magnetic resonant reflectivity curves.[20] For simulating the reflectance from an arbitrary layer stack, REMAGX can use either the Parratt algorithm[21] or a full matrix based magneto-optical description.[22] The former of the two algorithms is commonly used for standard, nonresonant x-ray reflectometry since the calculation is very fast and interface roughness is easily included analytically.[23] However the Parratt algorithm is not suited for resonant scattering at a magnetic active absorption edge in the soft x ray since it neglects the link of the $\sigma$ and $\pi$ eigenmodes ($\sigma \rightarrow \pi$ and $\pi \rightarrow \sigma$ scattering) within the layer stack (see, e.g., Ref. 24). To account for these processes properly, a full magneto-optical description based on $4 \times 4$ matrices is a possible solution. REMAGX uses the approach described in Ref. 22 to simulate the reflectivity from a layered sample. To account for interface roughness and allow local variations in the magneto-optical properties, the sample is sliced[25] into thin layers and each layer has its optical properties assigned according to the density profile. This slicing process is done automatically before each simulation and fitting iteration. It should be noted that this process allows introducing arbitrary variations in the magnetic properties in a very simple way. The use of the full optical matrix multiplication already causes an increase in the computation time by a factor of 10 compared to the Parratt algorithm but the necessity of slicing leads to an increase in several orders of magnitude depending on the number of slices. REMAGX provides different optimization algorithms for fitting XRMR data: besides the Simplex and Levenberg-Marquardt algorithms, an evolution strategy in form of a genetic algorithm (GA) fitting routine is available. GAs are especially well suited for fitting reflectivity curves with large numbers of free parameters or a parameter landscape with many local minima.[26,27] Here the structure determination of the sample used the layer thicknesses $d_i$ and roughnesses $\sigma_i$ as free parameter while the optical constants were derived from absorption experiments as described below and kept fixed during fitting. The magneto-optical profiles of the rotatable and pinned Mn moments were simulated by introducing a Gaussian shaped magneto-optical profile. The $z$ position, variance $\sigma^2$, and magneto-optical properties $\delta_{mag}$ and $\beta_{mag}$ of this artificial magnetic signal were free parameters of the fits of the magnetic asymmetries.

## III. ABSORPTION SPECTROSCOPY

Optical constants for both the relevant elements, Fe and Mn were obtained by measuring the near-edge x-ray absorption fine structure using TEY mode. The Mn x-ray absorption spectroscopy (XAS) was obtained from another sample prepared under identical conditions but without the ferromagnetic Fe layer thus providing a better signal from the MnPd. However, the Pt capping layer was retained to prevent oxidation. The sample was rotated to an incidence angle, $\Theta = 45°$, and the TEY and TFY were measured for each energy point using linearly polarized x rays. The resulting normalized Mn XAS $L$ edges are shown in Fig. 2(a). The spectrum shows a very narrow peak with two shoulders at the $L_3$ edge and a double-peak structure for the $L_2$ edge. This spectrum of manganese in MnPd clearly shows differences compared to reference spectra for metallic Mn.[28,29] The latter exhibits a broad $L_3$ peak without shoulders and a single $L_2$ peak which is narrower compared to the double-peak structure found here. The XAS spectrum of MnO on the other hand exhibits a multipletlike peak structure[30–32] similar to the one found here although the structures are less pronounced in MnPd. In MnO the manganese is in the $Mn^{2+}$ electronic configuration ($3d^5$) with localized electrons showing a typical multiplet structure.[33] However MnO XAS spectra reveal a pronounced peak at the low-energy shoulder, which is missing here for TEY and TFY spectra. This is a strong indication for the absence of an MnO like spectral contribution from the surface, which would be visible and more pronounced in the surface sensitive TEY mode. TFY on the other hand probes deep into the bulk and the corresponding spectrum is dominated by the bulk properties. The fact that TEY and TFY in Fig. 2(a) both show the same features at the $L_3$ and especially the double-peak structure at the $L_2$ confirms that indeed the

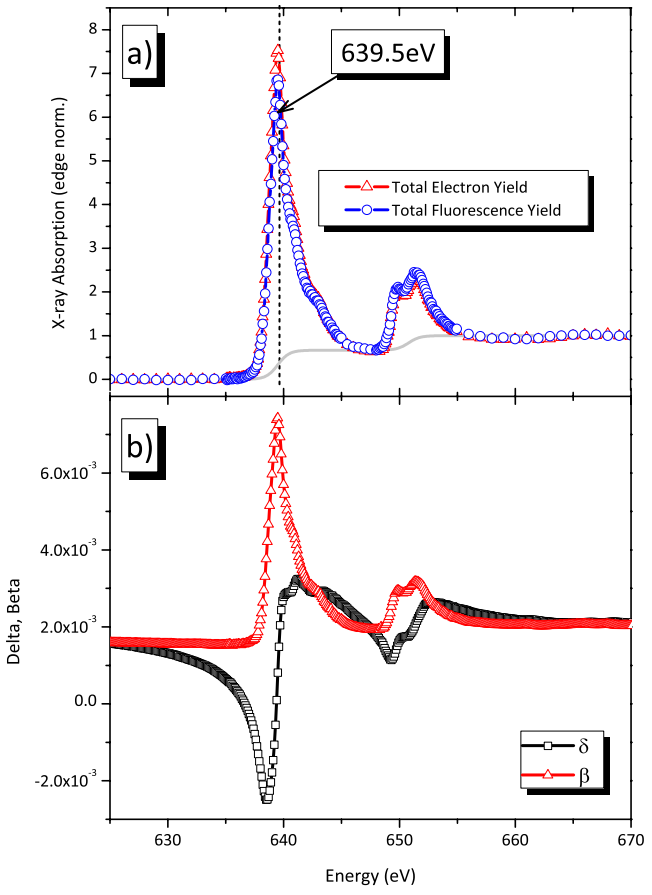


FIG. 2. (Color online) Manganese x-ray absorption near-edge spectrum measured by TEY and TFY at an angle of incidence of 45° using linearly polarized light. As can be seen, the surface sensitive TEY and the bulk dominated TFY have identical shapes proving that no surface oxidation took place. Most of the XRMR data were measured at 639.5 eV (marked). Figure 2(b) shows optical constants for $Mn_{52}Pd_{48}$. The imaginary part, $\beta$, is directly obtained from Fig. 2(a) while the real part, $\delta$, was derived by applying the Kramers-Kronig transform described in the text.

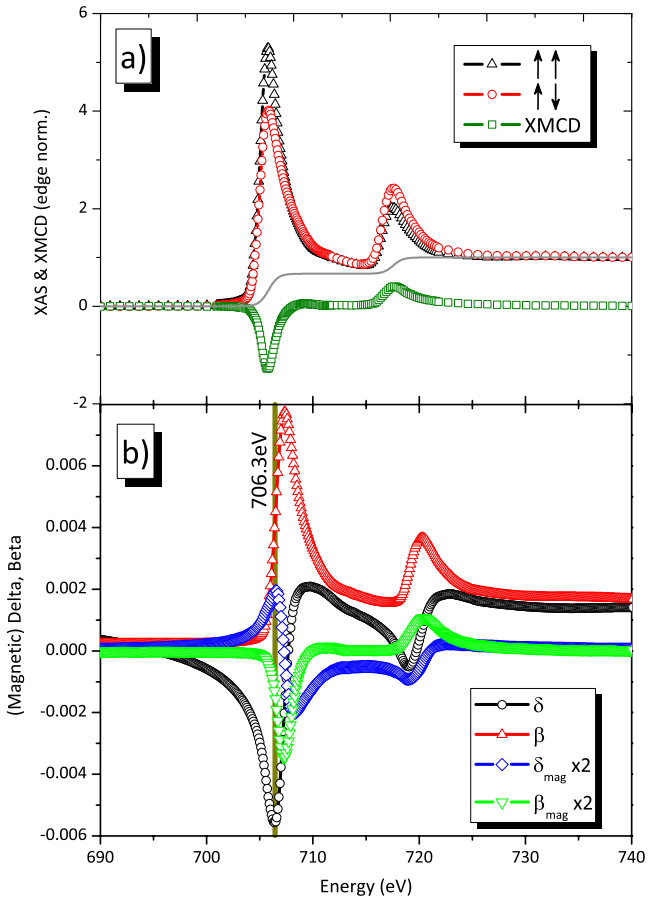


FIG. 3. (Color online) XMCD at the Fe edge measured for positive circular polarized light at an angle of incidence, $\Theta=45°$, by switching the magnetization direction at each energy point. The gray line represents the standard two-step background which has been subtracted for the sum-rule calculation. Figure 3(b) shows the optical (circle/triangle) and the magneto-optical (rhombus/triangle) constants derived from the TEY data of Fig. 3(a) using the Kramers-Kronig calculus described in the text.

bulk and the surface of the sample are the same and that surface oxidation is not the reason for the spectral shape in Fig. 2(a). The small height difference between the TEY and the TFY at high absorption values at the $L_3$ edge is due to the self-absorption (or saturation) effects, which are more pronounced in the TFY spectrum.[34,35] Reference data for MnPt (Ref. 30) closely resembles the shape of the Mn in MnPd. So it can be concluded that the Mn in MnPd is in a $Mn^{2+}$ configuration, not due to oxidation but due to the Pd. This finding is supported by the fact that Pd (and also Pt) has a considerably higher electronegativity of 2.20 (2.28 for Pt) compared to Mn which has only 1.51.[36] Anyway, the electrons are less localized than in MnO and accordingly the spectrum contains less structure. Next the XAS and XMCD of the Fe layer is investigated and discussed. Circularly polarized x rays with positive helicity were used for these measurements. A magnetic field of 85 mT was applied parallel and antiparallel with respect to the incident-beam direction to flip the magnetization of the sample at each energy value thus providing a XMCD difference signal. However to improve the signal-to-noise ratio for the TEY signal, the measurement has been carried out in remanence. The remanence of the sample is sufficient to allow such a procedure as can be seen from the VSM hysteresis in Fig. 1. Besides these changes, the same procedures and settings (namely, $\Theta=45°$) as for the Mn XAS were used. The resulting XAS for both field directions (indicated by $\uparrow\uparrow$ and $\uparrow\downarrow$) as well as the XMCD difference signal at the Fe $L$ edge of the sample are shown in Fig. 3(a). The spectrum corresponds very well in both shape and magnitude to the reference data for metallic Fe.[37,38] To quantify the magnetic spin and orbital moments, XMCD sum rules were applied. A standard two-step background, as indicated in the graph, was subtracted and the resulting curve was then integrated. The result was multiplied by the number of $3d$ holes which is $n_h=(10-n_{3d})$ and $n_{3d}=6.61$ for Fe which yields a hole number, $n_h=3.39$.[37] Furthermore, the result was corrected for the degree of circular polarization of the x rays (90%) and for the angle of incidence, $\Theta=45°$, and for the reduced remnant magnetization by a factor of 1.176 (see Fig. 1). The resulting corrected spin moment for the ferromagnetic Fe in the sample is $m_s$

$=(1.98\pm0.03)\mu_B$/atom and the orbital moment is $m_l$ $=(0.02\pm0.03)\mu_B$/atom. Both values are, within the error, in good agreement with reference data for Fe.[37]

## IV. OPTICAL CONSTANTS

Based on the Mn XAS and Fe XAS/XMCD data, the optical $(N=1-\delta+i\beta)$ and magneto-optical constants $\{n=N\pm(\delta_{mag}-i\beta_{mag})\cos(\vec{k},\vec{M})\}$ were derived using the Kramers-Kronig transform. Therefore the measured absorption data are edge normalized to get rid of measurement specific offsets and slopes and the resulting curve is fitted to tabulated scattering factors.[39,40] Here we follow the notation from Ref. 39. Subsequently a Kramers-Kronig calculus is performed to obtain the real part $f_1$ of the scattering factor.

Between the supporting points $f_{2i}=f_2(E_i)$ the scattering factor is approximated by a linear equation $f_2(E)=b_i+m_i\cdot E$. Here, $m_i$ is the slope of the function $f_2(E)$ between the energy $E_i$ and $E_{i+1}$ and $b_i$ is the corresponding axis intercept: $b_i=f_{2i}-m_i\cdot E_i$. The Kramers-Kronig relation then can be integrated exactly leading to

$$f_1(E_i) = Z + \frac{2}{\pi}\sum_i \int_{E_i}^{E_{i+1}} \frac{E'\cdot(b_i+m_i\cdot E')}{(E^2-E'^2)}dE'$$

$$= Z + \frac{2}{\pi}\sum_i \mathrm{Re}\left[-\frac{1}{2}b_i\ln(E^2-E'^2) - m_iE' + \frac{1}{2}\ln(E+E')Em_i - \frac{1}{2}\ln(E-E')Em_i\right]_{E_i}^{E_{i+1}}.$$

This solution especially avoids the singularity problem occurring by standard numerical integration methods and leads to smooth curves for sufficiently dense supporting points. The optical constants of both layers, Fe and MnPd, respectively, were calculated using this scheme.

The resulting $\delta$ and $\beta$ of $Mn_{52}Pd_{48}$ [derived from the TEY data in Fig. 2(a)] are shown in Fig. 2(b). The optical and magneto-optical constants for Fe are shown in Fig. 3(b). It has to be mentioned that the Mn $L_{2,3}$ magneto-optical constants could not be measured in a reliable way for Mn due to the thick Fe layer on top. We did not observe a significant TEY or TFY XMCD signal of the small interface related uncompensated Mn moments, buried below the thick Fe film on top. Therefore it was necessary to derive these Mn parameters directly from the magnetic reflectometry, which will be discussed later.

## V. RESULTS

To resolve the chemical structure of the sample, i.e., the layer thicknesses and interface roughness, resonant nonmagnetic reflectometry was measured for Mn using linear horizontal polarized x rays.[11] For Fe, XRMR close to the Fe $L_3$ edge at an energy of 706.3 eV was measured using positive circular polarized x rays. The sample magnetization was flipped for each angle of incidence by applying an external magnetic field of $\pm67$ mT. The resulting two reflectivity curves (circle/triangle) are shown in Fig. 4 along with the best-fit result from simulating the curves (dark gray/light gray solid lines). Note that the measured curve has been background corrected by $\cos(2\Theta)$ to account for strong diffuse scattering at this energy. The fit has been obtained by using the magneto-optical constants shown in Fig. 3(b). The roughness parameters derived from the fit at the Fe $L$ edge differ between 0.3 and 0.6 Å from the values derived at the Mn $L_3$ edge (see Ref. 11). This is below the resolution limit. The layer thicknesses on the other hand show slight variations. The Pt layer thickness obtained here is $d_{Pt}=20.3$ Å and the Fe layer thickness $d_{Fe}=80.4$ Å while it was 16.4 and 87.3 Å, respectively, in Ref. 11. This difference can be explained by the higher sensitivity to the upper Fe layer properties at this energy. At the Fe $L$ edge, the index of refraction exhibits a dramatic change at the Pt/Fe and Fe/MnP interface while at the Mn $L$ edge only the latter is changing. Therefore the Fe data are more sensitive to the Fe/Pt interface. With regard to the comparison with the Mn orientation it is good to keep in mind that magneto-optical constants with negative sign of the absorption at the Fe $L_3$ fit the data for positive circular polarized x rays properly.

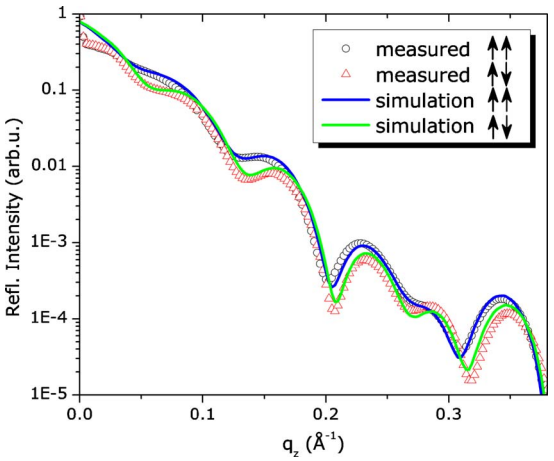


FIG. 4. (Color online) X-ray resonant magnetic reflectometry (black and red open circles) measured close to the Fe $L_3$ edge at an energy of 706.3 eV [compare Fig. 3(b)] using positive circular polarized x rays. The external magnetic field of 67 mT was flipped for each angle value to obtain the two curves. The blue and green curves are the best result from fitting a simulation to the data based on the optical and magneto-optical constants from Fig. 3(b) and the layer parameters (roughness and thickness) from Ref. 11.

With the structural information available, x-ray resonant magnetic reflectometry was measured for the Mn to obtain signals from rotatable and pinned uncompensated moments in the AF. Therefore the magnetic reflectivity was measured for both field directions by flipping the external field of $\pm67$ mT at each angle of incidence. Positive circularly polarized x rays are used and in addition the measurement was subsequently repeated for the opposite helicity. This method provides four different reflectivity curves according to the scheme: $\uparrow\uparrow$, $\uparrow\downarrow$, $\downarrow\uparrow$, and $\downarrow\downarrow$, where the first arrow represents the helicity of the x rays while the second indicates the direction of the magnetic field. The four resulting curves are shown in Fig. 5. From this set of data, the asymmetry signal related to rotatable Mn in the sample is obtained from *A*

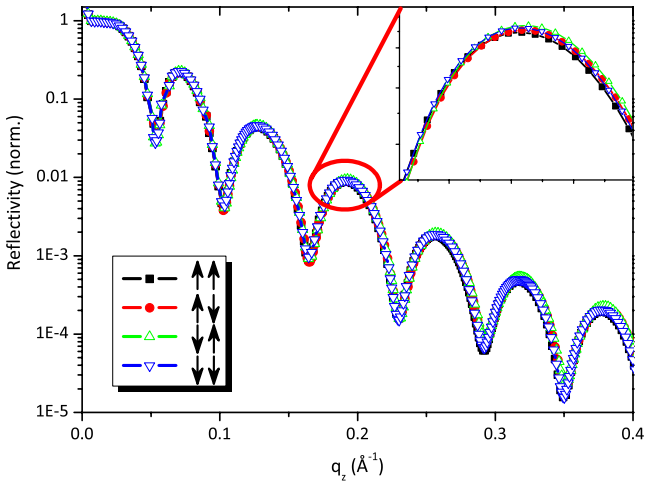


FIG. 5. (Color online) Magnetic resonant reflectivity of the sample measured at the Mn $L_3$ edge (639.5 eV) for all four possible alignments of polarization (first arrow) and magnetization (second arrow). The inset shows a closeup of the indicated region. Clear differences between the curves are visible.

$=(\uparrow\uparrow-\uparrow\downarrow)/(\uparrow\uparrow+\uparrow\downarrow)$. A large asymmetry signal of up to 15% from rotatable uncompensated Mn moments is found.[11] This clearly proves that rotatable Mn moments are present in the AF. The resulting magneto-optical profile indicating the position and width of the rotatable Mn is shown in Fig. 6. Rotatable Mn moments are only found in a ~4 Å wide region directly located at the interface. The width of this region correlates with the roughness of the interface suggesting that the neighborhood of Fe atoms is responsible for the Mn behavior. This interpretation is further stressed by the fact that Fe and rotatable Mn show exactly the same reversal behavior.[11] As mentioned above, no information about the magneto-optical constants of Mn was obtained from the absorption measurements, neither for the rotatable nor the pinned Mn. Instead, the magneto-optical constants for the rotatable moments were estimated from a reference XMCD signal of ferromagnetic Mn (Ref. 28) and then refined during the fitting process to match the magnitude of the moments here. To verify the $L_3$ finding, the magneto-optical profile of

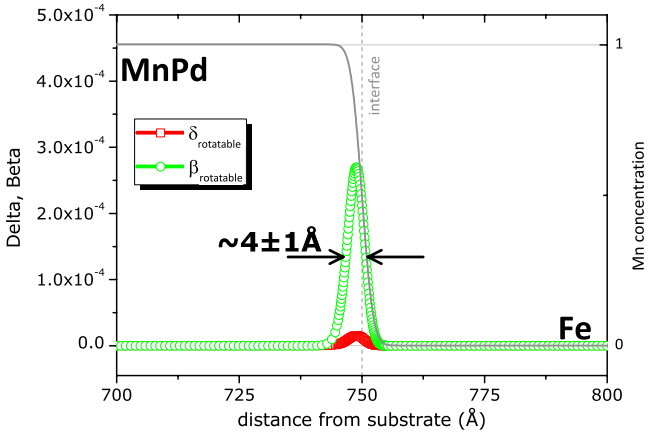


FIG. 6. (Color online) Magneto-optical profile of rotatable Mn moments measured at the Mn $L_3$ edge (639.5 eV).

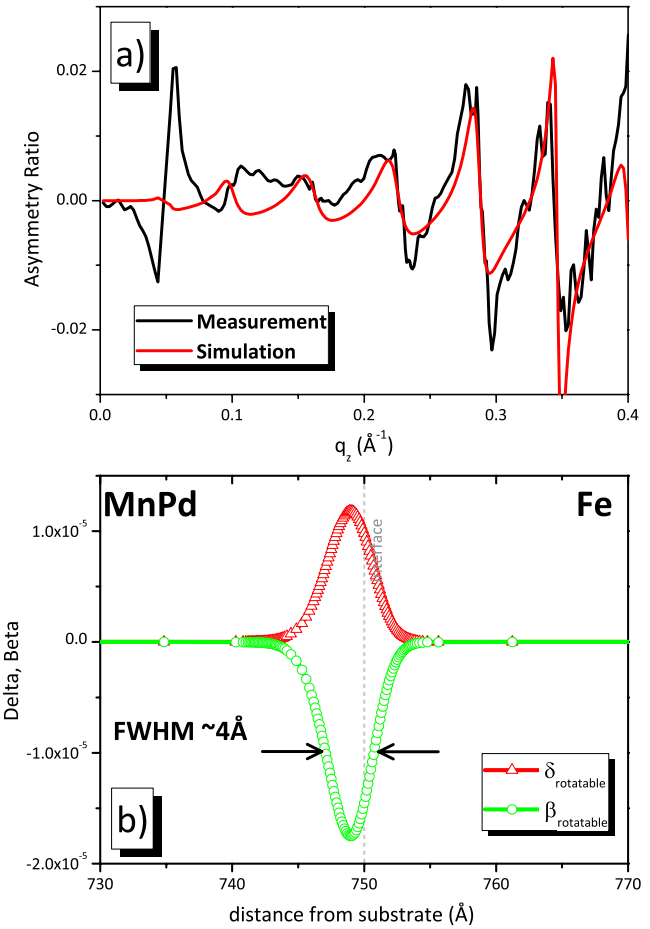


FIG. 7. (Color online) (a) shows the magnetic asymmetry (black line) resulting from rotatable uncompensated Mn moments measured at the $L_2$ edge of Mn (651.5 eV). The red curve shows the best-fit result obtained by fitting the magneto-optical constants and keeping the position and width of the distribution the same as in Ref. 11. (b) shows the magneto-optical profile of the rotatable uncompensated Mn moments at the $L_2$ edge of Mn which leads to the red curve in (a).

the rotatable Mn moments has also been fitted at the Mn $L_2$ edge. While the position and width of the distribution was kept fixed for the fitting process, $\delta_{mag}$ and $\beta_{mag}$ were refined. The measured curve along with the best fit is shown in Fig. 7(a). The signal is roughly a factor of 10 smaller than at the $L_3$ (Ref. 11) due to the reduced scattering cross section at the $L_2$ edge. Figure 7(b) shows the magneto-optical profile of the simulation result. The imaginary, i.e., absorptive part at the $L_2$ is negative and opposite in sign to that at the $L_3$ edge. But while the dispersive part, $\delta_{rotatable}$, is very small at the $L_3$, it is of nearly the same magnitude here. This can be used to check the agreement with the reference XMCD spectra from the literature by comparing the relative magnitude and sign of the two constants. Figure 8 shows the magneto-optical constants of ferromagnetic, metallic Mn from Ref. 28, which were initially used to fit the signal of the rotatable uncompensated Mn. As can be seen, the same relative signs and magnitudes for $\delta$ and $\beta$ are found from the reference data clearly proving that the shape of the XMCD spectrum of the rotatable, uncompensated Mn is of the same general form.

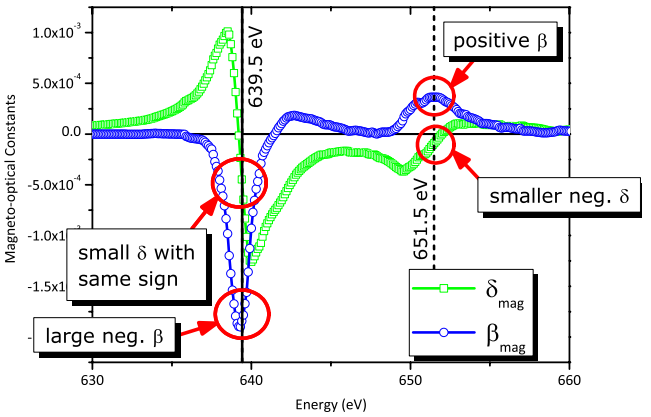


FIG. 8. (Color online) Magneto-optical constants of ferromagnetic, metallic Mn obtained from reference data (Ref. 28). The two energies where the XRMR measurements were carried out are indicated.

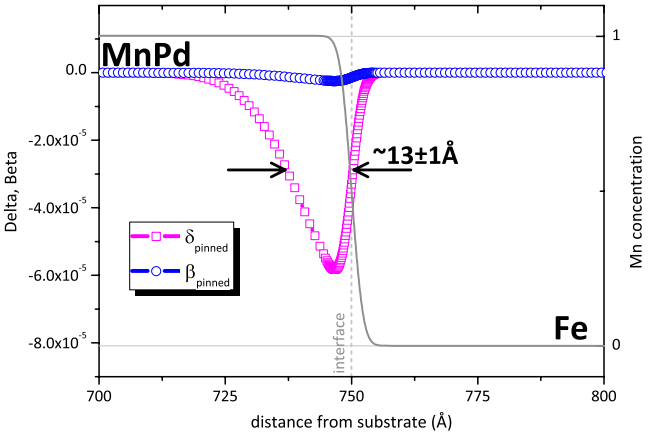


FIG. 9. (Color online) Magneto-optical profile associated to pinned uncompensated Mn moments in the sample.

Small differences in their relative magnitudes are very likely related to the digitalization process used to obtain the reference data. From this comparison the orientation of the rotatable Mn with respect to the ferromagnetic Fe on top can be derived. While the Fe XMCD of Fig. 3 has negative sign at the $L_3$ and positive at the $L_2$, and the Mn has a positive sign at the $L_3$ and a negative one at the $L_2$ for the absorptive part of the index of refraction although both were measured using positive circular polarized x rays. The obvious interpretation is that the Fe and rotatable Mn moments are oriented antiparallel with respect to each other. This is in agreement with the typical behavior of Fe and Mn coupling as found in FeMn alloys.[41,42] From investigations of ultrathin Mn on Fe films it is found that the Mn can couple antiferromagnetic[43] or ferromagnetic[44] to the Fe depending on the precise local configuration of the atoms.

The investigation of the magneto-optical constants of the pinned uncompensated Mn moments is complicated by the fact that their signal needs to be separated from the rotatable contribution. Therefore a different asymmetry calculus is necessary. By calculating the asymmetry using $A=(\uparrow\uparrow-\downarrow\downarrow)/(\uparrow\uparrow+\downarrow\downarrow)$ the rotatable contribution is blanked out because their net magnetization stays parallel to the incident x rays for both curves and the only remaining signal originates from the pinned moments. This calculus was applied to the data from Fig. 5 and a pinned asymmetry of 2.5% was found for Mn clearly proving the existence of such uncompensated pinned moments in the AF.[11] Since no information is available about the shape of the spectroscopic signal of pinned magnetic moments, the magneto-optical constants were set as free parameters of the fit. Nevertheless a good convergence of the fit was reached with reasonable values for the two constants.[11] The magneto-optical profile describing the position, distribution, and magnitude of the pinned uncompensated Mn in the AF is shown in Fig. 9. The pinned uncompensated Mn moments are located close to the interface in a region roughly 13 Å wide and slightly beneath the rotatable Mn. Besides the position, an unexpected relationship between $\delta$ and $\beta$ is found in the profile. While one would expect a large $\beta$, i.e., a maximum of the XMCD at the $L_3$ edge (also compare Fig. 6), the profile shows only a very small absorptive part. In fact, the dispersive part, $\delta$, dominates the profile. This effect might result from a modified shape and/or position of the magnetic spectra of the pinned Mn atoms as it is imposed, for example, by a change in the local chemical environment.

The coupling of the pinned moments is estimated by comparing the sign of the magneto-optical constants to ferromagnetic metallic Mn reference data. Figure 10 shows the magneto-optical constants of metallic Mn from Fig. 8 (from Ref. 28) together with four different simulations of the asymmetry signal from pinned uncompensated Mn. From the general shape of the XMCD curve, three different regions around the $L_3$ edge can be identified:

Before the $L_3$ edge, $\delta$ and $\beta$ have different sign and either $\beta$ is larger than $\delta$ (very close to the $L_3$) or they are of same magnitude but opposite sign. This region is marked green.

Directly on the $L_3$ (the maximum of the XMCD), $\beta$ is very large while $\delta$ is zero or close to it. The region is marked red in the figure. Behind the $L_3$ edge (blue), $\delta$ and $\beta$ have the same sign and their relative strength varies from being equal (closer to the $L_3$) to a large $\delta$ and small $\beta$ (right side of the blue region).

To verify that the method used here is sensitive enough to distinguish between these different cases, four different simulations with varying $\delta/\beta$ ratio and sign are shown in Fig. 10. The magnetic asymmetry from the pinned Mn moments was simulated based on four different relations between the two magneto-optical constants: $\delta$ and $\beta$ have different sign (Case 1), $\beta$ is large and $\delta$ much smaller (Case 2), same magnitude and sign (Case 3), and a large $\delta$ and small $\beta$ (Case 4). The last case is the best result from fitting the pinned asymmetry data according to its $\chi^2$. Although the XMCD data are obtained for ferromagnetic Mn, the shape of the curve is of general character so it is justified to assume that the pinned Mn would yield similar relations for $\delta$ and $\beta$ (sign and relative magnitude). The fact that the pinned asymmetry fits to a spectra with negative XMCD at the $L_3$ (thus $\delta > \beta$) means that the pinned moments point along the positive field direction. According to the data from Fig. 3, this implies parallel coupling with respect to the Fe during the field cooling process. So the coupling of the pinned Mn mo-

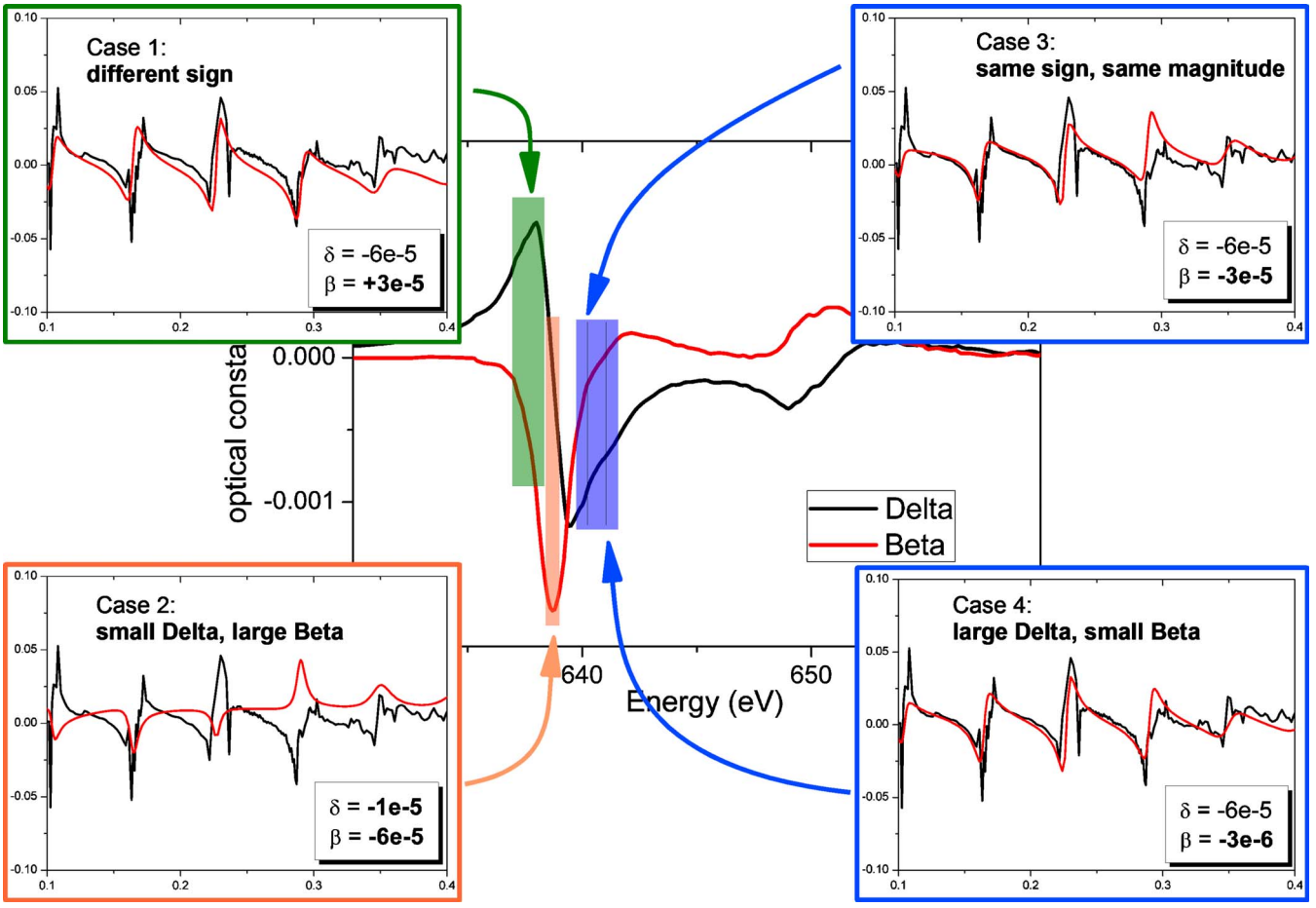


FIG. 10. (Color online) The graph in the middle shows the magneto-optical constants of metallic ferromagnetic Mn obtained from the literature (Ref. 28). Marked in the graph are three regions, before the $L_3$ (green), directly on the $L_3$ (red), and behind the $L_3$ (blue) corresponding to unique relations of $\delta$ and $\beta$. The four graphs arranged around the magneto-optical constant plot represent simulations of the pinned asymmetry based on these different $\delta/\beta$ constellations. The black curve in each figure is the measured data. Case 4 is the best-fit result and was used throughout this work.

ments is parallel to the Fe but antiparallel to the rotatable Mn which is compatible with the expected spin configuration of $a$-axis MnPd.[17] In contrast, antiparallel coupling has been reported in CoO and IrMn.[14] This might result from the different spin structure of these antiferromagnets compared to the one in MnPd or to the fact that the system investigated there has a perpendicular magnetization.

## VI. SUMMARY

An epitaxially grown Fe/MnPd exchange-bias sample was investigated using XMCD and XRMR to identify uncompensated moments in the AF and their relative coupling with respect to the ferromagnetic Fe. High quality XAS and XMCD spectra of the Fe $L$ and Mn $L$ edges were measured to derive the optical and magneto-optical constants of both elements. The Mn XAS shows that Mn in MnPd behaves more like $Mn^{2+}$ than like metallic Mn. The XRMR investigation at the Mn $L_3$ and $L_2$ edge reveals the existence of rotatable uncompensated Mn in a $(4 \pm 1)$ Å broad region directly at the AF/F interface. Since the interface roughness is of the same size, this means that only 1–2 monolayers of Mn are ferromagnetic. Comparing the signs and magnitudes of the magneto-optical constants with reference XMCD spectra for metallic Mn, an antiparallel orientation of these moments with respect to the F is found. A XRMR signal which can be associated to pinned uncompensated magnetic Mn moments was observed in the sample. These moments are also located close to the AF-F interface but in a much broader region of ~13 Å. The orientation of these moments with respect to Fe and rotatable Mn during the field cooling process can be derived by comparing the found magneto-optical constants with literature data of metallic Mn. Their orientation during the field cooling process was antiparallel with respect to the neighboring rotatable Mn and parallel to the Fe layer on top.

## ACKNOWLEDGMENTS

The authors thank V. Ferreras Paz, B. Zada, and W. Mahler for support during the beamtime at BESSY II. Work at UW was supported by DOE/BES under Contract No. ER45987.

*seb@brueck-online.com
†kannanmk@u.washington.edu

[1] J. Nogués and I. K. Schuller, J. Magn. Magn. Mater. **192**, 203 (1999).
[2] A. E. Berkowitz and K. Takano, J. Magn. Magn. Mater. **200**, 552 (1999).
[3] F. Radu and H. Zabel, *Magnetic Heterostructures*, Springer Tracts in Modern Physics Vol. 227 (Springer, Berlin/Heidelberg, 2008), pp. 97–184.
[4] S. Brück, J. Sort, V. Baltz, S. Suriñach, J. S. Muñoz, B. Dieny, M. D. Baró, and J. Nogués, Adv. Mater. **17**, 2978 (2005).
[5] I. V. Roshchin, O. Petracic, R. Morales, Z. P. Li, X. Batlle, and I. K. Schuller, Europhys. Lett. **71**, 297 (2005).
[6] A. Hoffmann, J. W. Seo, M. R. Fitzsimmons, H. Siegwart, J. Fompeyrine, J. P. Locquet, J. A. Dura, and C. F. Majkrzak, Phys. Rev. B **66**, 220406(R) (2002).
[7] P. Kappenberger, S. Martin, Y. Pellmont, H. J. Hug, J. B. Kortright, O. Hellwig, and E. E. Fullerton, Phys. Rev. Lett. **91**, 267202 (2003).
[8] H. Ohldag, A. Scholl, F. Nolting, E. Arenholz, S. Maat, A. T. Young, M. Carey, and J. Stöhr, Phys. Rev. Lett. **91**, 017203 (2003).
[9] F. Offi, W. Kuch, L. I. Chelaru, K. Fukumoto, M. Kotsugi, and J. Kirschner, Phys. Rev. B **67**, 094419 (2003).
[10] S. Roy, M. R. Fitzsimmons, S. Park, M. Dorn, O. Petracic, I. V. Roshchin, Z. P. Li, X. Batlle, R. Morales, A. Misra, X. Zhang, K. Chesnel, J. B. Kortright, S. K. Sinha, and I. K. Schuller, Phys. Rev. Lett. **95**, 047201 (2005).
[11] S. Brück, G. Schütz, E. Goering, X. Ji, and K. M. Krishnan, Phys. Rev. Lett. **101**, 126402 (2008).
[12] S. Roy, C. Sanchez-Hanke, S. Park, M. R. Fitzsimmons, Y. J. Tang, J. I. Hong, D. J. Smith, B. J. Taylor, X. Liu, M. B. Maple, A. E. Berkowitz, C. C. Kao, and S. K. Sinha, Phys. Rev. B **75**, 014442 (2007).
[13] K. Takano, R. H. Kodama, A. E. Berkowitz, W. Cao, and G. Thomas, Phys. Rev. Lett. **79**, 1130 (1997).
[14] I. Schmid, P. Kappenberger, O. Hellwig, M. J. Carey, E. E. Fullerton, and H. J. Hug, EPL **81**, 17001 (2008).
[15] M. R. Fitzsimmons, B. J. Kirby, S. Roy, Z. P. Li, I. V. Roshchin, S. K. Sinha, and I. K. Schuller, Phys. Rev. B **75**, 214412 (2007).
[16] P. Colombi, D. K. Agnihotri, V. E. Asadchikov, E. Bontempi, D. K. Bowen, C. H. Chang, L. E. Depero, M. Farnworth, T. Fujimoto, A. Gibaud, M. Jergel, M. Krumrey, T. A. Lafford, A. Lamperti, T. Ma, R. J. Matyi, M. Meduna, S. Milita, K. Sakurai, L. Shabel'nikov, A. Ulyanenkov, A. V. der Lee, and C. Wiemer, J. Appl. Crystallogr. **41**, 143 (2008).
[17] N. Cheng, J. Ahn, and K. M. Krishnan, J. Appl. Phys. **89**, 6597 (2001).
[18] P. Blomqvist, K. M. Krishnan, and D. E. McCready, J. Appl. Phys. **95**, 8019 (2004).
[19] S. Brück, S. Bauknecht, B. Ludescher, E. Goering, and G. Schütz, Rev. Sci. Instrum. **79**, 083109 (2008).
[20] S. Macke, S. Brück, and E. Goering, "REMAGX—X-ray magnetic reflectivity tool," www.mf.mpg.de/remagx.html
[21] L. G. Parratt, Phys. Rev. **95**, 359 (1954).
[22] J. Zak, E. R. Moog, C. Liu, and S. D. Bader, Phys. Rev. B **43**, 6423 (1991).
[23] L. Névot and P. Croce, Rev. Phys. Appl. **15**, 761 (1980).
[24] S. A. Stepanov and S. K. Sinha, Phys. Rev. B **61**, 15302 (2000).
[25] S. A. Stepanov and R. Köhler, J. Appl. Phys. **76**, 7809 (1994).
[26] A. Ulyanenkov and S. Sobolewski, J. Phys. D **38**, A235 (2005).
[27] J. Tiilikainen, V. Bosund, M. Mattila, T. Hakkarainen, J. Sormunen, and H. Lipsanen, J. Phys. D **40**, 4259 (2007).
[28] W. L. O'Brien and B. P. Tonner, Phys. Rev. B **50**, 2963 (1994).
[29] B. T. Thole, R. D. Cowan, G. A. Sawatzky, J. Fink, and J. C. Fuggle, Phys. Rev. B **31**, 6856 (1985).
[30] J. Fujii, F. Borgatti, G. Panaccione, M. Hochstrasser, F. Maccherozzi, G. Rossi, and G. van der Laan, Phys. Rev. B **73**, 214444 (2006).
[31] S. Andrieu, E. Foy, H. Fischer, M. Alnot, F. Chevrier, G. Krill, and M. Piecuch, Phys. Rev. B **58**, 8210 (1998).
[32] H. J. Lee, G. Kim, D. H. Kim, J. S. Kang, C. L. Zhang, S. W. Cheong, J. H. Shim, S. Lee, H. Lee, J. Y. Kim, B. H. Kim, and B. I. Min, J. Phys.: Condens. Matter **20**, 295203 (2008).
[33] C. Mitra, Z. Hu, P. Raychaudhuri, S. Wirth, S. I. Csiszar, H. H. Hsieh, H. J. Lin, C. T. Chen, and L. H. Tjeng, Phys. Rev. B **67**, 092404 (2003).
[34] S. Eisebitt, T. Böske, J. E. Rubensson, and W. Eberhardt, Phys. Rev. B **47**, 14103 (1993).
[35] L. Tröger, D. Arvanitis, K. Baberschke, H. Michaelis, U. Grimm, and E. Zschech, Phys. Rev. B **46**, 3283 (1992).
[36] J. Mullay, *Electronegativity*, Structure and Bonding Vol. 66 (Springer, Berlin/Heidelberg, 1987), pp. 1–25.
[37] C. T. Chen, Y. U. Idzerda, H. J. Lin, N. V. Smith, G. Meigs, E. Chaban, G. H. Ho, E. Pellegrin, and F. Sette, Phys. Rev. Lett. **75**, 152 (1995).
[38] E. Goering, S. Gold, and A. Bayer, Appl. Phys. A: Mater. Sci. Process. **78**, 855 (2004).
[39] B. L. Henke, E. M. Gullikson, and J. C. Davis, At. Data Nucl. Data Tables **54**, 181 (1993).
[40] C. T. Chantler, J. Phys. Chem. Ref. Data **29**, 597 (2000).
[41] J. Kouvel and J. Kasper, J. Phys. Chem. Solids **24**, 529 (1963).
[42] H. Umebayashi and Y. Ishikawa, J. Phys. Soc. Jpn. **21**, 1281 (1966).
[43] J. Dresselhaus, D. Spanke, F. U. Hillebrecht, E. Kisker, G. van der Laan, J. B. Goedkoop, and N. B. Brookes, Phys. Rev. B **56**, 5461 (1997).
[44] S. Andrieu, M. Finazzi, F. Yubero, H. Fischer, P. Arcade, F. Chevrier, K. Hricovini, G. Krill, and M. Piecuch, J. Magn. Magn. Mater. **165**, 191 (1997).